

“Synthetic” DSC perfusion MRI with adjustable acquisition parameters in brain tumors using dynamic spin-and-gradient-echo echo planar imaging

Francesco Sanvito^{1,2}, Jingwen Yao^{1,2}, Nicholas S. Cho¹⁻⁴, Catalina Raymond^{1,2}, Donatello Telesca⁵, Whitney B. Pope², Richard G. Everson⁶, Noriko Salamon², Jerrold L. Boxerman⁷, Timothy F. Cloughesy⁸, Benjamin M. Ellingson^{1,2,4,6,9}*

ABSTRACT

BACKGROUND AND PURPOSE: Normalized relative cerebral blood volume (nrCBV) and percentage of signal recovery (PSR) computed from dynamic susceptibility contrast (DSC) perfusion imaging are useful biomarkers for differential diagnosis and treatment response assessment in brain tumors. However, their measurements are dependent on DSC acquisition factors, and CBV-optimized protocols technically differ from PSR-optimized protocols. This study aimed to generate “synthetic” DSC data with adjustable synthetic acquisition parameters using dual-echo gradient-echo (GE) DSC datasets extracted from dynamic spin-and-gradient-echo echo planar imaging (dynamic SAGE-EPI). Synthetic DSC was aimed at: 1) simultaneously create nrCBV and PSR maps using optimal sequence parameters, 2) compare DSC datasets with heterogeneous external cohorts, and 3) assess the impact of acquisition factors on DSC metrics.

MATERIALS AND METHODS: Thirty-eight patients with contrast-enhancing brain tumors were prospectively imaged with dynamic SAGE-EPI during a non-preloaded single-dose contrast injection and included in this cross-sectional study. Multiple synthetic DSC curves with desired pulse sequence parameters were generated using the Bloch equations applied to the dual-echo GE data extracted from dynamic SAGE-EPI datasets, with or without optional preload simulation.

RESULTS: Dynamic SAGE-EPI allowed for simultaneous generation of CBV-optimized and PSR-optimized DSC datasets with a single contrast injection, while PSR computation from guideline-compliant CBV-optimized protocols resulted in rank variations within the cohort (Spearman’s $\rho=0.83-0.89$, i.e. 31%-21% rank variation). Treatment-naïve glioblastoma exhibited lower parameter-matched PSR compared to the external cohorts of treatment-naïve primary CNS lymphomas (PCNSL) ($p<0.0001$), supporting a role of synthetic DSC for multicenter comparisons. Acquisition factors highly impacted PSR, and nrCBV without leakage correction also showed parameter-dependence, although less pronounced. However, this dependence was remarkably mitigated by post-hoc leakage correction.

CONCLUSIONS: Dynamic SAGE-EPI allows for simultaneous generation of CBV-optimized and PSR-optimized DSC data with one acquisition and a single contrast injection, facilitating the use of a single perfusion protocol for all DSC applications. This approach may also be useful for comparisons of perfusion metrics across heterogeneous multicenter datasets, as it facilitates post-hoc harmonization.

ABBREVIATIONS: DSC = dynamic susceptibility contrast; FA = flip angle; GBCA = gadolinium-based contrast agent; GBM = glioblastoma; GE = gradient echo; IDH = isocitrate dehydrogenase; IDH^m = IDH-mutant; IDH^{wt} = IDH-wild-type; 1p19q^{cod} = 1p19q codeleted; 1p19q^{int} = 1p19q intact; MRI = magnetic resonance imaging; PCNSL = primary CNS lymphoma; PSR = percentage of signal recovery; Rec = recurrent; SAGE-EPI = spin-and-gradient-echo echo planar imaging; CBV = cerebral blood volume; nrCBV = normalized relative CBV; ROI = region of interest; TE = echo time; TN = treatment-naïve; TR = repetition time.

Received month day, year; accepted after revision month day, year.

From the UCLA Brain Tumor Imaging Laboratory (BTIL), Center for Computer Vision and Imaging Biomarkers, and Department of Radiological Sciences, (F.S., J.Y., N.S.C., C.R., B.M.E.), Department of Neurosurgery (R.G.E., B.M.E.), Department of Neurology (T.F.C.), Department of Radiological Sciences (W.B.P., N.S.), Department of Psychiatry and Biobehavioral Sciences (B.M.E.), Medical Scientist Training Program (N.S.C.), David Geffen School of Medicine, Department of Bioengineering, Henry Samueli School of Engineering and Applied Science (N.S.C., B.M.E.), Department of Biostatistics (D.T.), University of California Los Angeles, Los Angeles, CA, USA; from the Department of Diagnostic Imaging (J.L.B.), Warren Alpert Medical School, Brown University, Providence, RI, USA.

Funding: This project was funded by the following grants: NIH NCI F30CA284809 (N.S.C.), NIH NIGMS T32GM008042 (N.S.C.), NIH NCI R01CA270027 (B.M.E.), NIH NCI R01CA279984 (B.M.E.), DoD CA20029 (B.M.E.), DoD CA220732 (B.M.E.).

Disclosures: B.M.E. owns the patent for dynamic SAGE-EPI (patent: US 11,378,638 B2). B.M.E. is on the advisory board of Carthera, Chimerix, Erasca, Global Coalition for Adaptive Research, Imaging Endpoints, Medicenna, Voiant/MedQIA, Monteris, Neosoma, Orbus Therapeutics, Sagimet Biosciences, Sapience Therapeutics, Servier Pharmaceuticals, SonALAsense, Sumitomo Dainippon Pharma Oncology, Third Rock Ventures, and is a paid advisor and consultant for Medicenna, Voiant/MedQIA, Neosoma, Servier Pharmaceuticals, Siemens, Janssen, Imaging Endpoints, Kazia, VBL, Oncoceutics/Chimerix, Carthera, Erasca, Sumitomo Dainippon Pharma Oncology, ImmunoGenesis, Orbus Therapeutics, Ellipses Pharma, Monteris, Global Coalition for Adaptive Research (GCAR), Alpheus Medical, Inc., SonALAsense, Third Rock Ventures, Curtana Pharma, and Sagimet Biosciences. Grant funding is from Siemens, Servier/Agios, Neosoma, and Janssen. T.F.C. is cofounder, major stock holder, consultant and board member of Katmai Pharmaceuticals, holds stock for Erasca, member of the board and paid consultant for the 501c3 Global Coalition for Adaptive Research, holds stock in Chimerix and receives milestone payments and possible future royalties, member of the scientific advisory board for Break Through Cancer, member of the scientific advisory board for Cure Brain Cancer Foundation, has provided paid consulting services to Third Rock, Symbio, Mundipharma, Tango BlueRock, Vida Ventures, Lista Therapeutics, Stemline, Novartis, Roche, SonalAsense, Sagimet, Clinical Care Options, Ideology Health, Servier, Jubilant, Immvira, Gan & Lee, BrainStorm, Katmai, Sapience, Inovio, Vigeo Therapeutics, DNATrix, Tyme, SDP, Kintara, Bayer, Merck, Boehringer Ingelheim, VBL, Amgen, Kiyatec, Bayer, Abbvie, VBI, Deciphera, VBL, Agios, Novocure, Medscape and has contracts with UCLA for the Brain Tumor Program with Servier, Roche, VBI, Merck, Novartis, BMS, In8bio. The Regents of the University of California (T.F.C. employer) has licensed intellectual property co-invented by T.F.C. to Katmai Pharmaceuticals.

SUMMARY SECTION

PREVIOUS LITERATURE: Dynamic susceptibility contrast (DSC) perfusion MRI is routinely used to evaluate the normalized relative cerebral blood volume (nrCBV) and percentage of signal recovery (PSR) in brain tumors. nrCBV and PSR are useful biomarkers for differential diagnosis and treatment response assessment in brain tumors. However, CBV-optimized DSC acquisition protocols have different acquisition parameters compared to PSR-optimized protocols, which makes it impractical to obtain simultaneous nrCBV and PSR measurements within the same MRI session. Additionally, heterogeneity in acquisition parameters across institutions is known to pose limitations in the universalizability of the quantification and interpretation of these DSC metrics.

KEY FINDINGS: Dual-echo DSC extracted from dynamic SAGE-EPI allows to generate synthetic DSC data with adjustable synthetic acquisition parameters (i.e., flip angle, echo time, repetition time, and preload simulation). Synthetic DSC experiments confirmed that nrCBV and PSR measurements are dependent on acquisition parameters. Comparisons with external cohorts showed that parameter-matched synthetic PSR in glioblastoma is significantly different from external cohorts of PCNSL.

KNOWLEDGE ADVANCEMENT: Synthetic DSC can simultaneously generate CBV-optimized and PSR-optimized DSC data with one acquisition and a single contrast injection, facilitating accurate nrCBV and PSR measurements within the same MRI session. Synthetic DSC has also the potential to achieve post-hoc harmonization of DSC parameters to improve the comparisons across heterogeneous multicenter datasets.

INTRODUCTION

Dynamic susceptibility contrast (DSC) perfusion MRI of the brain¹ provides non-invasive information about vascularity, including measures of regional cerebral blood volume (CBV), which has been shown to correlate with vascular density in brain tissue¹⁻³. In addition, from DSC time-intensity curves it is possible to compute the percentage of signal recovery (PSR), whose contrast appears to arise from the complex interplay of multiple tissue factors, including cellular architecture, vascular permeability, and vascular architecture⁴⁻⁸. CBV⁹⁻¹² and PSR^{6,13} can inform the clinical management of brain tumors. Both have been shown to predict the molecular profile of gliomas, differentiate progressive disease from pseudoprogression during active treatment monitoring,¹⁴⁻¹⁹ and aid in differentiating between several tumor types including glioma, primary CNS lymphoma (PCNSL), and metastasis^{2,8,20-26}. Although CBV is more widely employed and is overall considered a more robust metric for most of these applications, PSR may be superior to CBV when distinguishing PCNSL from other tumor types^{20,21}.

Although both CBV and PSR provide potentially important information about tumor biology, obtaining optimal CBV and PSR measurements with a single-echo DSC acquisition is not possible, since CBV-optimized protocols^{27,28} differ significantly from PSR-optimized protocols^{21,22}. Indeed, DSC time-intensity curves are influenced by acquisition factors that impact the degree of relative T_2^* - and T_1 -weighting, including pulse sequence parameters (flip angle [FA], echo time [TE], and repetition time [TR]) and preload administration (P+ or P-). CBV-optimized protocols adopt various strategies to *reduce* the relative T_1 -weighting (e.g., low FA or P+) and increase CBV accuracy^{27,29}. Conversely, PSR-optimized protocols *maintain* T_1 -weighting (i.e., high FA and P-)^{21,22} so that DSC signal reflects the overall balance between T_1 and T_2^* post-bolus effects that depend on tissue factors^{4,5,7}. Therefore, either repeat single-echo DSC acquisitions are needed if both PSR-optimized and CBV-optimized protocols are desired, which doubles the scan time and the gadolinium-based contrast agent (GBCA) dose, or either CBV or PSR must be prioritized with a single acquisition.

Additionally, such dependency of DSC time-intensity curves upon acquisition factors causes a remarkable challenge in the standardization of CBV and PSR for clinical applications. Indeed, the heterogeneity in acquisition protocols across institutions has limited the availability of reliable thresholds for universal interpretation of DSC metrics. Of note, data quantifying the impact of acquisition parameters on DSC metrics *in-vivo* are scarce, and limited to the comparisons between P- and P+ protocols³⁰⁻³², as repeat DSC experiments are influenced by GBCA injections acting as preloads.

In this study, we propose to use the dual-echo gradient-echo (GE) datasets extracted from dynamic spin-and-gradient-echo echoplanar imaging (SAGE-EPI) to obtain “synthetic” DSC time-intensity curves with adjustable acquisition parameters (i.e., FA, TE, TR, and preload simulation), to overcome the limitations linked to parameter dependency in traditional single-echo DSC sequences. First, we anticipate that dual-echo GE will permit *simultaneous* acquisition of CBV-optimized and PSR-optimized synthetic DSC datasets, eliminating the need for double GBCA injection and repeated acquisitions, and we will evaluate the differences between these protocols. Second, we hypothesize that synthetic DSC datasets could represent a strategy for improving the generalizability of DSC by bypassing acquisition parameter heterogeneity across institutions. To test this, we will compare PSR values from synthetic DSC in our treatment-naïve glioblastoma cohort to external cohorts of PCNSL, after parameter-matching. Third, we propose that synthetic DSC can provide a framework to test the impact of acquisition factors (FA, TE, TR, P+/P-) on CBV and PSR *in-vivo*, which can be used to inform future recommendations on single-echo DSC protocols.

MATERIALS AND METHODS

Patient Selection

Patients with brain tumors were imaged prospectively as part of two research studies approved by the institutional review board (IRB#14-001261 and #21-000514) for which they provided written informed consent. Patients on study IRB #14-001261 were imaged between April 2015 and October 2020, and patients on study #21-000514 from October 2021 to June 2022. For the present study, we screened all the consecutive patients to select the ones with the following inclusion criteria: availability of dynamic SAGE-EPI datasets, contrast-enhancing tumor, histopathological diagnosis of adult-type glioma (either recurrent or treatment-naïve). The presence of excessive susceptibility artifacts affecting the tumor region in dynamic SAGE-EPI was an exclusion criterion. A STROBE checklist was followed to design the study and report the results (see **Suppl. Material**).

Magnetic Resonance Imaging

Magnetic resonance imaging was performed on a 3T Siemens Prisma (Siemens Healthineers) in compliance with the current standardized brain tumor imaging protocol (BTIP)^{28,33}. Perfusion imaging was performed with a custom dynamic SAGE-EPI sequence (patent US 11,378,638 B2)^{3,7,34,35} with injection of one bolus of Gadavist® (Gadobutrol, Bayer) (~0.1ml/kg) at a rate of ~4 ml/s, as per guidelines³⁶. Dynamic SAGE-EPI included two gradient echoes (TE₁=14ms, TE₂=34.1ms), an asymmetric spin echo (TE₃=58.0ms) and a spin echo (TE₄=92.4ms) using the following acquisition parameters: TR=2.0s, matrix size=240x218mm, GRAPPA=3, voxel size 1.875x1.875x5mm, 19 axial slices, 90 timepoints.

Image Analysis

The two gradient echoes (Echo1 and Echo2) were motion-corrected with FSL *mcflirt* (University of Oxford, <https://fsl.fmrib.ox.ac.uk/fsl/>), and the Bloch equations were used to compute the transverse relaxation rate over time, $R_2^*(t)$ [s⁻¹]^{7,37} (**Fig.1, Suppl.Eq.1**). The T₁-weighted signal contribution of the gradient echoes ($T_1w(t)$) was obtained by extrapolating the signal at TE=0ms, as previously described^{7,37}, and used to calculate the longitudinal relaxation rate over time $R_1(t)$ [s⁻¹] by assuming a fixed T₁ (T₁₀) [s] for the tissue (**Fig.1, Suppl.Eq.2**; refer to **Suppl.Fig.1** for analyses reporting on the robustness of the methodology with respect to T₁₀ assumptions). When desired, $R_1(t)$ and $R_2^*(t)$ were adjusted to simulate a full-dose preload administration (P+) (**Fig.1, Suppl.Eq.3**), by assuming that a second bolus administration would cause the same change in relaxation rates $\Delta R_1(t)$ and $\Delta R_2^*(t)$.

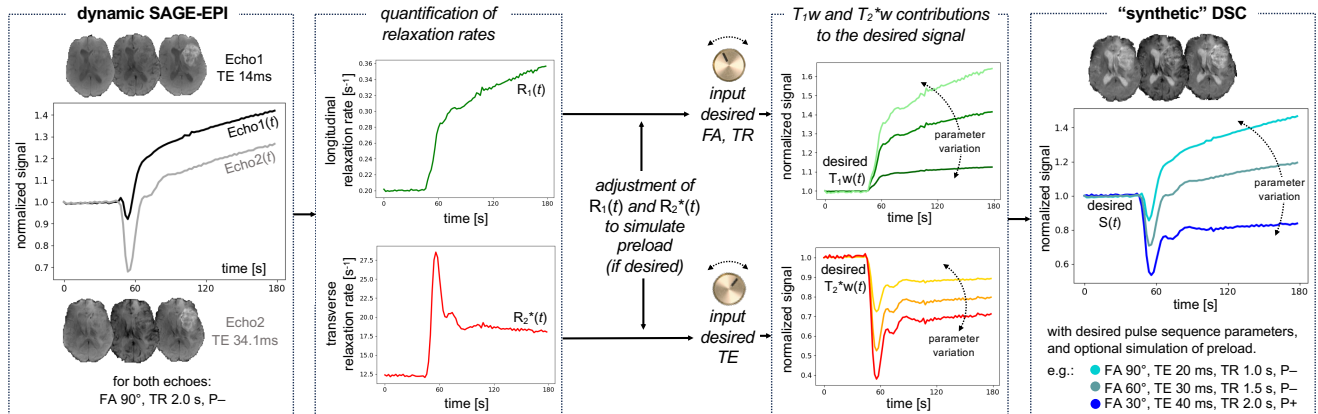


FIG 1. Image processing pipeline to obtain voxel-wise synthetic DSC datasets from dynamic SAGE-EPI. Echo1 (GE, TE=14ms) and echo2 (GE, TE=34.1ms) were used to compute $R_1(t)$ and $R_2^*(t)$. If desired, $R_1(t)$ and $R_2^*(t)$ were adjusted to simulate a preload administration. The desired $T_1w(t)$ component of the synthetic DSC was calculated from $R_1(t)$ by inputting the desired FA and TR in the Bloch equations. Similarly, the desired $T_2^*w(t)$ component of the synthetic DSC was calculated from $R_2^*(t)$ by inputting the desired TE in the Bloch equations. Finally, the synthetic DSC time-intensity curve is obtained by combining the desired $T_1w(t)$ and $T_2^*w(t)$. The final plot shows how different parameter combinations generate synthetic DSC time-intensity curves with different relative T₁- and T₂*-weighting.

$R_1(t)$ and $R_2^*(t)$ were then used in the Bloch equations to respectively compute the *desired* T₁-weighted component ($T_1w_{desired}(t)$) and T₂*-weighted component ($T_2^*w_{desired}(t)$) of the synthetic DSC with desired FA, TE, and TR (**Fig.1, Suppl.Eq.4-5**). Finally, the “synthetic” DSC time-intensity curve ($S_{desired}(t)$) was obtained by multiplying $T_1w_{desired}(t)$ and $T_2^*w_{desired}(t)$ (**Fig.1, Suppl.Eq.6**).

For inter-protocol comparisons, synthetic DSC datasets were generated with: one guideline-compliant CBV-optimized protocol with simulated preload (FA 60°, TE 30ms, TR 1.5s, P+) ²⁷, one guideline-compliant CBV-optimized protocol without simulated preload (FA 30°, TE 30ms, TR 1.5s, P-) ²⁷, and one PSR-optimized protocol (FA 90°, TE 30ms, TR 1.5s, P-) ²¹. For comparisons with external cohorts acquired at 3T, synthetic DSC datasets were generated with acquisition parameters matching the ones reported in Cindil *et al.* ²¹ (FA 90°, TE 30ms, TR 1.5s, P-, acquisition time 1min 23s) and Wang *et al.* ²² (FA 90°, TE 30ms, TR 1.6s, *both* P- and P+, acquisition time 1min 36s). Note that we truncated our synthetic DSC time-intensity curves (3min) to match the external cohorts (1min 23s and 1min 36s), because the signal recovery depends on the acquisition time. Finally, to explore the impact of acquisition protocols on DSC metrics, we recursively generated synthetic DSC datasets while changing one parameter at the time.

$S_{desired}(t)$ was used to compute $\Delta R_{2, *single_echo}(t)$ [s^{-1}] as in classic single-echo DSC studies, and rCBV maps were computed by integrating the positive values of $\Delta R_{2, *single_echo}(t)$ (Suppl.Eq.7, Suppl.Fig.2A-B)³⁷. This step was repeated without model-based leakage correction, with bidirectional leakage correction³⁸, and with Boxerman-Schmainda-Weisskoff (BSW) leakage correction³⁹. Finally, nrCBV maps were generated with normalization to the contralateral white matter (Suppl.Eq.7)¹². PSR maps were generated from $S_{desired}(t)$ without leakage correction, as previously described (Suppl.Eq.8, Suppl.Fig.2C)^{7,20}.

A neuroradiologist with 8 years of experience in neuroimaging (F.S.) used digital subtraction maps of pre- and post-contrast T₁-weighted images to segment the contrast-enhancing component of the lesion^{7,40}. Segmentations were registered to the perfusion space using FSL *flirt*.

Statistical Analyses

For comparisons across protocols, Spearman's correlation coefficient (ρ)⁴¹ and two-way mixed single score intraclass correlation coefficient (ICC3)⁴² of median tumor PSR and nrCBV were obtained, and interpreted as in dedicated statistical articles^{41,42}. ρ tests whether the ranks of the tumor values are maintained across protocols, which influences the diagnostic performance of DSC metrics. The percent variation in ranks introduced by protocol variations was calculated as $(1-\rho^2) \times 100\%$ (Suppl.Eq.9). ICC3 tests the agreement of different protocols on the exact value of a certain DSC metric⁴². The comparisons with external cohorts focused on PSR only, because the technical variability of PSR is entirely due to acquisition factors, without confounding aspects such as the leakage correction fit and the contralateral white matter signal. The PSR mean and standard deviation of our treatment-naïve glioblastoma subgroup was calculated and compared to the mean and standard deviation of external cohorts with two-sample t-tests. Neither non-parametric tests nor ROC curve computation were feasible, because the individual tumor-specific values of PSR of the external cohorts were not available.

RESULTS

Thirty-eight patients met the inclusion and exclusion criteria for the study (see the flow-chart in Suppl.Fig.3), with tumors of various grades and molecular status, either treatment-naïve or recurrent (Table 1). All recurrent lesions showed histopathologically-defined recurrent tumor (i.e., actively proliferating tumor cells, with or without evidence of treatment effects) in surgical specimens obtained in the weeks following the MRI acquisition. Of note, some analyses from this cohort were previously reported in an article with a substantially different aim and design⁷.

Table 1: Demographic, clinical, and pathological features of the study cohort.

Characteristics of the study cohort (n=38)	
Age (years, mean \pm SD)	54.4 \pm 14.0
Sex category (F)	
F	11 (28.9%)
M	27 (71.1%)
Main location	
Frontal	11 (28.9%)
Parietal	8 (21.1%)
Temporal	9 (23.7%)
WM/deep GM	4 (10.5%)
Multiple lobes	6 (15.8%)
Treatment status	
Treatment-naïve	14 (36.8%)
Recurrent	24 (63.2%)
Grade	
2	4 (10.5%)
3	4 (10.5%)
4	30 (78.9%)
Molecular status	
IDH ^m 1p19q ^{int}	10 (26.3%)
IDH ^m 1p19q ^{cod}	3 (7.9%)
IDH ^{wt}	25 (65.8%)

Plots of time-intensity curves from synthetic DSC with varying parameters were generated and a visual assessment revealed that the curve shapes changed consistently with previous findings (i.e., showing reduced relative T₁-weighting with lower FA, longer TE, longer TR, and with preload simulation P+) (Fig.2).

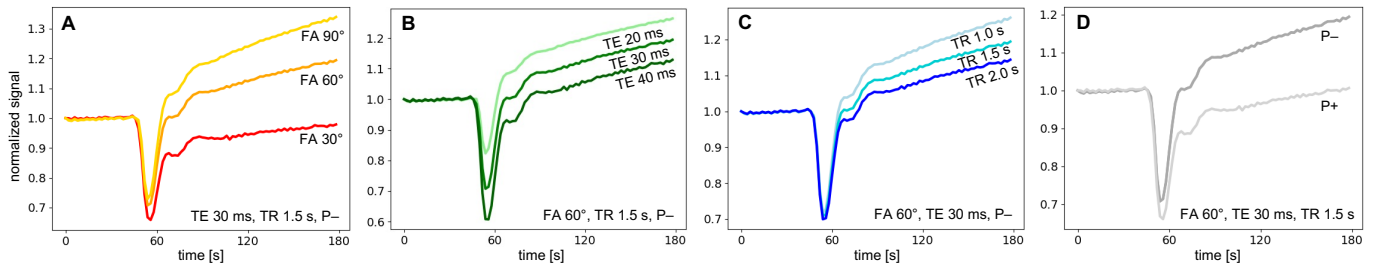


FIG 2. Examples of synthetic DSC time-intensity curves obtained with varying acquisition parameters in one representative tumor. As expected, lower FA (A), longer TE (B), longer TR (C), and the presence of preload simulation P+ (D) determined a reduced relative T1-weighting and an increased relative T2*-weighting in the time-intensity curve. This was observed in all tumors. Note that, while the median tumor signal was plotted for the visualization of this representative case, the synthetic DSC pipeline was performed voxel-wise for all the analyses.

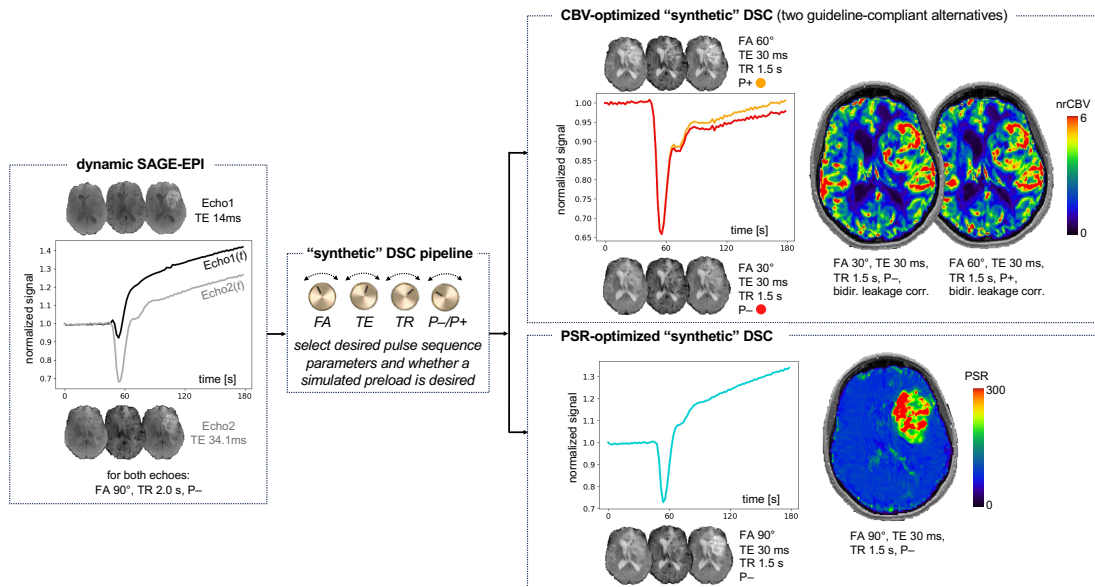


FIG 3. Clinical application of synthetic DSC to simultaneously generate CBV-optimized and PSR-optimized DSC datasets.

Comparison between CBV-optimized and PSR-optimized protocols

Synthetic DSC permits generation of CBV-optimized and PSR-optimized DSC datasets from single acquisitions, which can be used in the clinical setting to simultaneously obtain nrCBV and PSR maps from synthetic optimal protocols (**Fig.3**). Conversely, obtaining PSR from CBV-optimized protocols can lead to inaccurate results. Median tumor PSR values computed with CBV-optimized protocols (FA 30° P- and FA 60° P+) had poor agreement (ICC3=0.20 and ICC3=0.34, respectively) with those computed with the PSR-optimized protocol (FA 90° P-), and showed 31% variation in ranks ($\rho=0.83$) for FA 30° P- and 21% variation in ranks ($\rho=0.89$) for FA 60° P+ (**Fig.4A**). Representative cases (tumors corresponding to the 20th, 40th, 60th, and 80th PSR percentile of our cohort) show how PSR maps from CBV-optimized protocols can yield different ranks compared to PSR-optimized ones (**Fig.4E-H**). Notably, the agreement of PSR values between the two CBV-optimized protocols was only “good” (ICC3=0.79), and also introduced rank variations (21%, $\rho=0.89$, **Fig.4B**).

Results suggested that nrCBV may be less influenced than PSR by acquisition factors, especially after bidirectional leakage correction³⁸, with excellent agreement between PSR-optimized and CBV-optimized protocols (ICC3=0.96 and ICC3=0.97, respectively, **Fig.4C**), and with nearly perfect agreement between the two CBV-optimized protocols (ICC3=0.99, **Fig.4D**). BSW leakage correction³⁹ yielded almost similar results (**Suppl.Fig.4A-B**). nrCBV without leakage correction had only a “good” agreement between PSR-optimized and CBV-optimized protocols (ICC3=0.89 and ICC=0.91, respectively, **Suppl.Fig.4C**) and an excellent agreement between the two CBV-optimized protocols (ICC3=0.97, **Suppl.Fig.4D**).

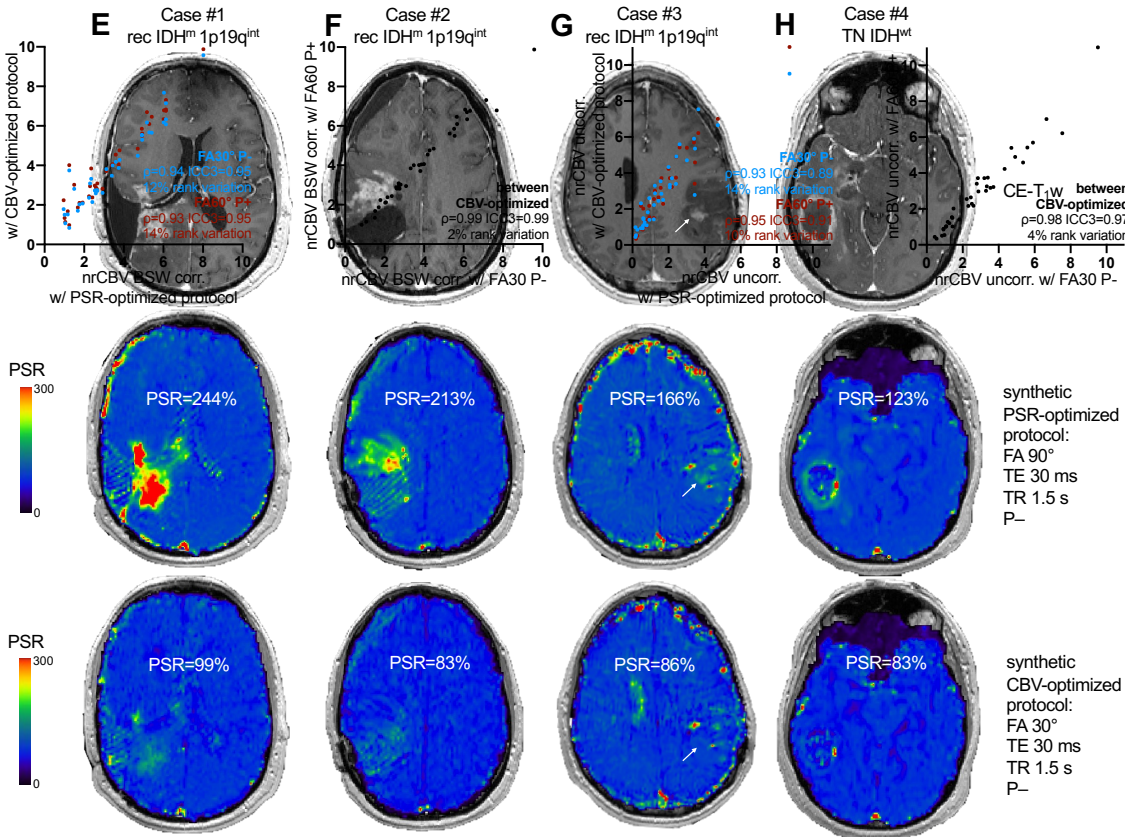
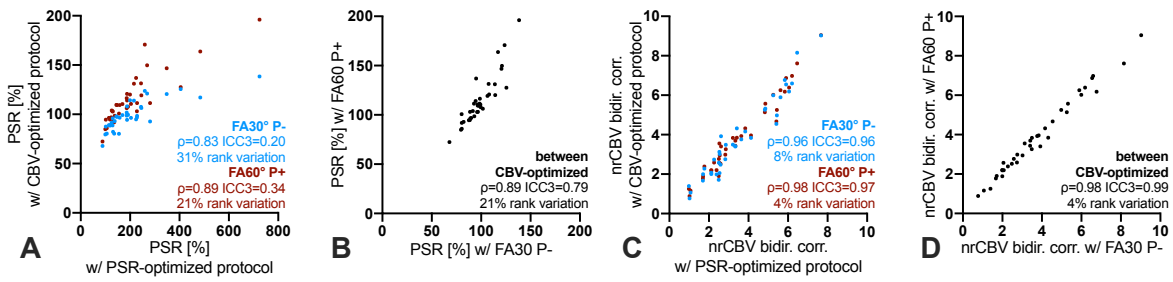


FIG 4. Comparisons of DSC metrics obtained with CBV- and PSR-optimized synthetic DSC protocols. PSR values (A, B) were strongly influenced by the acquisition factors, which impacted not only on the PSR value (reflected in the ICC3 test), but also on the ranks (reflected in the ρ value). nrCBV values with bidirectional leakage correction (C, D) were less influenced by the acquisition factors both in terms of agreement and rank consistency. Of note, the two CBV-optimized protocols yielded nrCBV values with nearly perfect agreement (D). Panels E-H show representative PSR maps cases of lesions corresponding to the 20th, 40th, 60th, and 80th PSR percentile of our cohort, along with the median PSR tumor value. CBV-optimized protocols not only yield different PSR values, but also sometimes result in different ranks of the lesion within the cohort. For instance, the median values of case #2 and #3 swapped ranks when moving from PSR-optimized to CBV-optimized protocols.

Comparison with external cohorts

Results demonstrate the ability for synthetic DSC to generate datasets with consistent acquisition parameters to external cohorts, which may be useful for putting contemporary studies into historic context. For example, synthetic parameter-matched PSR values from our cohort of treatment-naïve IDH^{wt} glioblastomas were lower than the cohort of treatment-naïve PCNSL ($104.5 \pm 26.5\%$ vs $164.1 \pm 37.0\%$ $p < 0.0001$, Fig.5A) reported by Cindil *et al.*²¹, and not statistically different from their reported glioblastoma cohort ($104.5 \pm 26.5\%$ vs $95.3 \pm 20.1\%$ $p = 0.26$, Fig.5A). As for Wang *et al.*²², synthetic parameter-matched PSR (P-) from our glioblastoma cohort yielded significantly lower PSR values compared to their PCNSL cohort acquired without preload ($108.3 \pm 26.8\%$ vs $163.0 \pm 90.0\%$ $p < 0.0001$, Fig.5B). After preload adjustment (P+), our cohort showed PSR values overlapping with their PCNSL cohort acquired with preload ($89.4 \pm 12.3\%$ vs $70.0 \pm 71.0\%$ $p = 0.03$, Fig.5C). While there remained a statistically significant difference between tumor groups, the overlap would arguably result in poor diagnostic performance. Suppl.Tab.1 reports clinical characteristics of the external cohorts, as well as details regarding imaging acquisition and analysis.

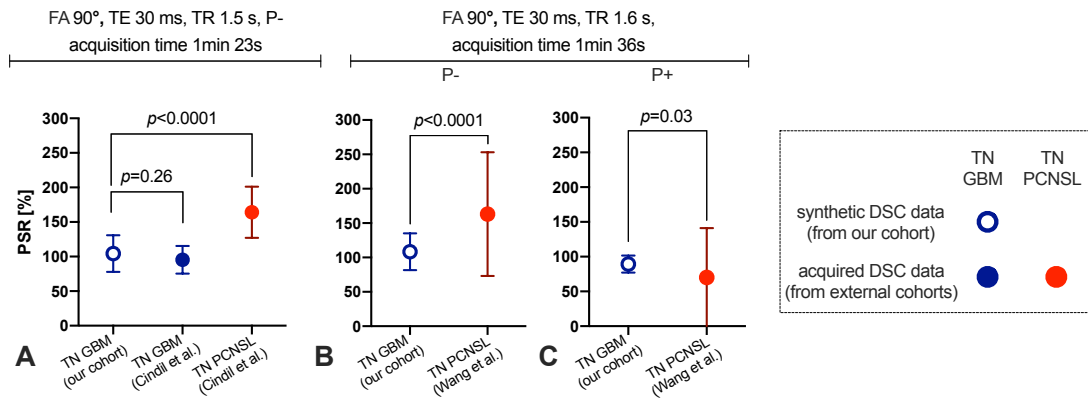


FIG 5. Clinical application of synthetic DSC to compare cohorts with different acquisition parameters. Median tumor PSR from our treatment-naïve glioblastoma cohort were lower than the PCNSL cohort reported by Cindil *et al.*²¹, and not different from their glioblastoma cohort (A). Similarly, without preload (P-), median tumor PSR from our treatment-naïve glioblastoma cohort were lower than the PCNSL cohort reported by Wang *et al.*²². With preload, median tumor PSR from our treatment-naïve glioblastoma cohort overlapped with the other PCNSL cohort reported by Wang *et al.*²². GBM = glioblastoma, PCNSL = primary CNS lymphoma, TN = treatment-naïve.

Impact of acquisition factors on DSC metrics

When varying acquisition parameters to assess of the impact of acquisition factors on DSC metrics *in-vivo*, results showed that median tumor PSR values progressively decreased when lowering FA, increasing TE, increasing TR, and when adding a simulated preload (P+) (Fig.6A-B). Altering acquisition factors not only caused a remarkable change in PSR values but also affect their ranks within the cohort, suggesting measures of PSR and interpretation are highly dependent on the acquisition parameters. Similarly, median nrCBV values without leakage correction tended to increase when lowering FA, increasing TE, increasing TR, and when adding a simulated preload (P+) (Fig.6C-D), which also effected the rank order among patients. Unlike PSR, however, nrCBV changes appear less predictable in terms of extent and directionality due to the interplay of the signal in the white matter, which is used for normalization. Bidirectional leakage correction remarkably mitigated the impact of acquisition factors on nrCBV estimates (Fig.6E-F). For reference, the BSW leakage correction showed comparable results (Suppl.Fig.5).

DISCUSSION

The current study proposes a novel methodology that generates multiple synthetic DSC datasets with adjustable pulse sequence parameters and optional preload simulation from a *single* dynamic SAGE-EPI sequence with a *single bolus* of contrast agent. Building on previous work showing how to disentangle T₁ and T₂* contributions to DSC from *in-vivo* dual-echo data^{7,37,43}, this is the first study proposing the usage of these disentangled signals to compute a new combined signal with adjustable acquisition parameters.

First, the current study demonstrates the ability for dynamic dual-echo GE DSC extracted from dynamic SAGE-EPI to synthesize CBV-optimized and PSR-optimized DSC datasets in a single experiment. While PSR can technically be computed from CBV-optimized acquisitions, its usefulness may be limited by the weak relative T₁-weighting of CBV-optimized acquisitions. Consistent with this hypothesis, data from the current study showed that PSR measurements from CBV-optimized protocols have poor agreement with measurements obtained with the recommended PSR-optimized protocols including consistency of ranks across protocols, suggesting this may negatively impact not only accuracy but also diagnostic performance. Importantly, even PSR measurements computed with two different guideline-compliant CBV-optimized protocols only had “good” agreement (not excellent nor perfect), thus limiting the universalizability of diagnostic cutoffs given this dependence on acquisition parameters. Our results are consistent with previous studies suggesting that PSR should be computed from PSR-optimized protocols, since the diagnostic utility of PSR from PSR-optimized acquisitions is well documented. For instance, AUC ranged 0.88-0.98 across studies^{8,21,22} for the differentiation of PCNSL from glioblastoma, when using a PSR-optimized protocol (high FA, P-). Conversely, in other cohorts, PSR differences between PCNSL and glioblastoma were reportedly either attenuated (AUC=0.82) or nullified (AUC=0.53) when using CBV-optimized and/or preloaded protocols. Of note, only one study reported a very high diagnostic performance of PSR in distinguishing PCNSL using a preloaded protocol²⁶. Overall, simultaneous PSR- and CBV-optimized synthetic protocols using dynamic dual-echo GE saves scan time and eliminates the need for double GBCA dose compared to duplicate experiments. Moreover, analyzing dynamic dual-echo GE is the only feasible methodology to obtain DCE in addition to PSR-optimized DSC and CBV-optimized DSC⁷. Indeed, single-echo acquisition schemes would not be suited to obtain all three, since both DCE and PSR-optimized DSC should be non-preloaded.

In addition to generating CBV- and PSR-optimized measurements, the current study demonstrates a framework for comparing prospectively acquired DSC data with external or historic data that was acquired under varying acquisition parameters. For example, comparison of parameter-matched PSR values in the current study cohort of treatment-naïve glioblastoma with PSR values from external cohorts were able to replicate similar PSR differences reported in the original articles. In clinical trials, inter-institution heterogeneity and lack of standardization is one of main factors why DSC is excluded from the evaluation of treatment response in clinical trials, as per RANO criteria⁴⁴, although this technique has been used to monitor treated glioblastomas for decades^{1,27,45,46}. Thus, synthetic DSC using

dynamic dual-echo GE or SAGE-EPI can potentially allow real-time comparisons to external and historic cohorts through synthesis of specific acquisition parameters, and more generally, allows for better uniformity and standardization in multicenter studies. Of note, dynamic dual-echo GE and the historic cohorts must be acquired at the same field strength for this application.

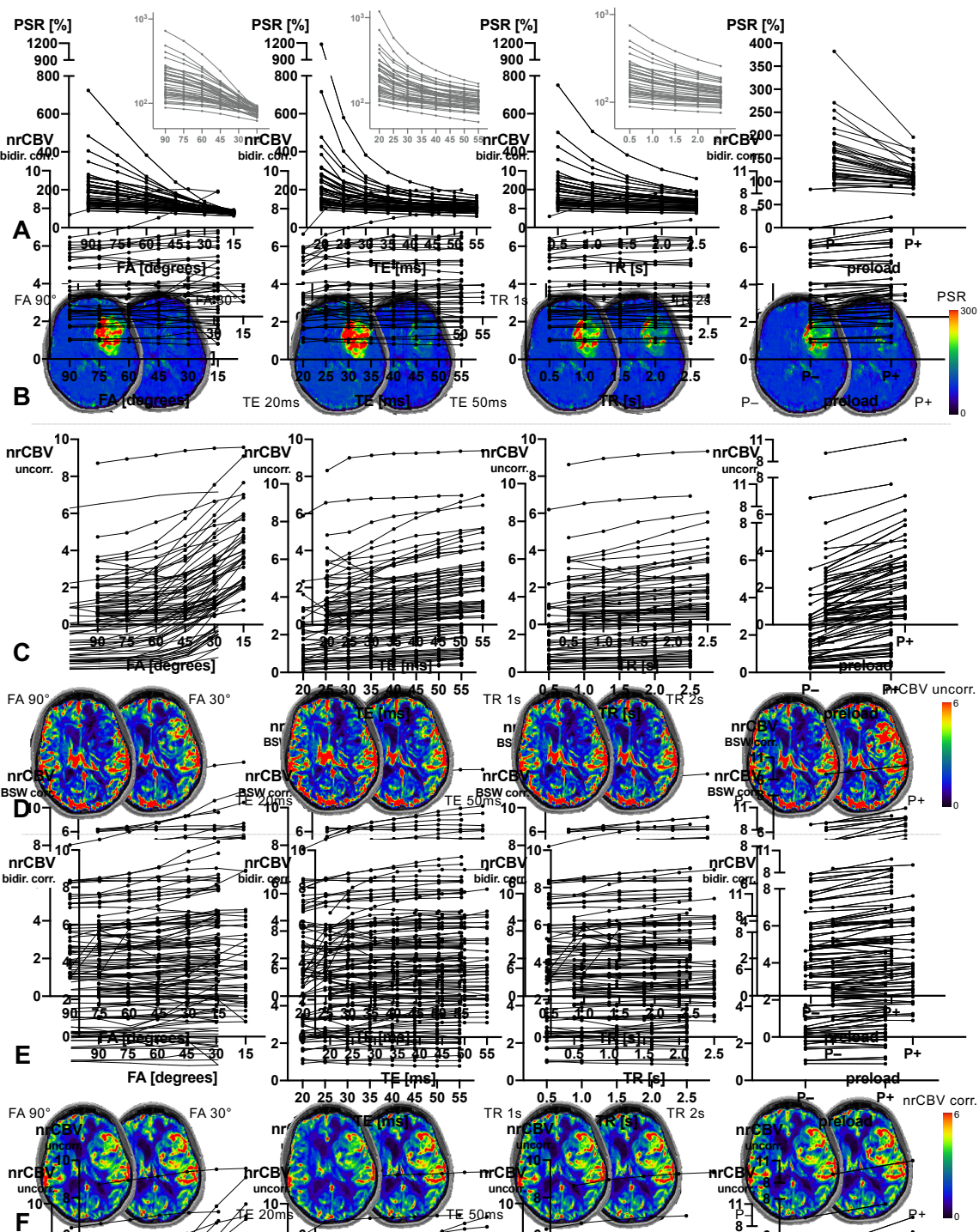


FIG 6. Research application of synthetic DSC to assess the impact of acquisition parameters on quantitative DSC metrics. Median tumor PSR and nrCBV were obtained from each subject, while systematically varying pulse sequence parameters and preload adjustment. Acquisition parameters were varied one at the time, and the “default” parameters were as follows: FA 60° TE 30ms TR 1.5s P-. PSR was highly sensitive to acquisition factors, as shown in both dot plots (A, including linear scaling in black and log-transformed scaling in grey) and representative voxelwise maps (B). Varying parameters not only influenced PSR values, but also the relative ranks of the subjects within the cohort. Dot plots (C) and voxelwise maps (D) of uncorrected nrCBV demonstrate nrCBV variations with acquisition factors, which are remarkably mitigated by model-based bidirectional leakage correction (E, F).

Furthermore, synthetic DSC may represent a tool for investigating optimal DSC parameters for single-echo protocols aimed at specific clinical applications. Future studies may systematically permute synthetic acquisition parameters to find the optimal combination that can maximize PSR differences between PCNSL and glioblastoma, or maximize CBV differences between progression and

pseudoprogression, or maximize the correlations between DSC metrics and histopathological findings such as vessel density. Other studies have proposed to investigate optimal DSC parameters by using digital reference objects (DROs) obtained from simulated *in-silico* analyses and validated with *in-vivo* datasets^{47–49}. Compared to the DRO approach, the synthetic DSC approach would have the advantage of being both agnostic to any biophysical assumptions needed to model the simulated tissue structures, and not being restricted to the disease category represented in the DRO training cohort (i.e., glioblastoma). On the other hand, it would have the disadvantage of *not* providing ground truth model-derived tissue characteristics (e.g., vessel density, cell density) to test the accuracy of perfusion metrics.

Limitations

Some potential limitations should be addressed. First, we did not prospectively obtain a pre-contrast T₁ map, so an estimated value of T₁₀ was chosen. However, simulated data suggested the absolute error derived from the assumed T₁₀ estimation was minimal. Future studies should perform pre-contrast T₁ mapping to improve accuracy. Secondly, the proposed preload adjustment assumes that a second bolus of GBCA causes the same change in longitudinal and transverse relaxation rates as the first bolus. This assumption is overall justifiable for the longitudinal relaxation rate under the Tofts generalized kinetic model⁵⁰, if an equal-dose bolus is injected close to the time of dynamic equilibrium. As for the transverse relaxation rate, this assumption is to be considered a simplification and it probably introduces some degree of inaccuracy that is not easily quantifiable, because the T₂* effects are highly dependent on the tissue geometry^{4,7,50,51}. Future studies may employ two consecutive DSC acquisitions (a non-preloaded dual-echo as first, and a preloaded one as second) to quantify the potential inaccuracy of our proposed synthetic preload. Additionally, the current study had no available prospective dynamic SAGE-EPI datasets from patients with PCNSL, which would allow direct testing of the diagnostic performance of synthetic DSC using various parameters. Finally, the estimates of PSR are highly dependent on the duration of the “tail” of the post-injection DSC curve. When comparing to external cohorts, this issue was mitigated by truncating the duration of the time-intensity curves to match the acquisition time of the external cohort. Future studies should model the post-bolus signal and directly define PSR based on this model to lessen the dependency on the duration of data acquired after contrast injection. Finally, the long TR of our sequence may result in a reduced signal-to-noise ratio of the acquired T₁-weighted component in presence or high GBCA concentrations. Future studies may implement simultaneous multi-slice to shorten the TR and address this limitation.

CONCLUSIONS

The dual-echo GE datasets extracted from dynamic SAGE-EPI allow for direct synthesis of multiple DSC datasets with adjustable acquisition parameters and preload simulations. This method allows for simultaneous generation of CBV-optimized and PSR-optimized measurements with a single injection and acquisition, facilitating the use of a single perfusion protocol for all DSC parameters. Additionally, synthetic DSC from dynamic SAGE-EPI allows for real-time comparison to historic and external datasets acquired with variable acquisition schemes, increasing the rigor of prospective DSC studies in brain tumors.

ACKNOWLEDGMENTS

None.

REFERENCES

1. Shiroishi, M. S. *et al.* Principles of T₂*-weighted dynamic susceptibility contrast MRI technique in brain tumor imaging. *J. Magn. Reson. Imaging* **41**, 296–313 (2015).
2. Zhang, J. *et al.* Clinical applications of contrast-enhanced perfusion MRI techniques in gliomas: Recent advances and current challenges. *Contrast Media Mol. Imaging* **2017**, (2017).
3. Chakhoyan, A. *et al.* Validation of vessel size imaging (VSI) in high-grade human gliomas using magnetic resonance imaging, image-guided biopsies, and quantitative immunohistochemistry. *Sci. Rep.* **9**, 2846 (2019).
4. Semmineh, N. B. *et al.* Assessing tumor cytoarchitecture using multiecho DSC-MRI derived measures of the transverse relaxivity at tracer equilibrium (TRATE). *Magn. Reson. Med.* **74**, 772–784 (2015).
5. Quarles, C. C., Gochberg, D. F., Gore, J. C. & Yankeelov, T. E. A theoretical framework to model DSC-MRI data acquired in the presence of contrast agent extravasation. *Phys. Med. Biol.* **54**, 5749–5766 (2009).
6. Pons-Escoda, A. *et al.* Differentiating IDH-mutant astrocytomas and 1p19q-codeleted oligodendrogliomas using DSC-PWI: high performance through cerebral blood volume and percentage of signal recovery percentiles. *Eur. Radiol.* (2024). doi:10.1007/s00330-024-10611-z
7. Sanvito, F. *et al.* Simultaneous quantification of perfusion, permeability, and leakage effects in brain gliomas using dynamic spin-and-gradient-echo echoplanar imaging MRI. *Eur. Radiol.* (2023). doi:10.1007/s00330-023-10215-z
8. Mangla, R. *et al.* Percentage signal recovery derived from MR dynamic susceptibility contrast imaging is useful to differentiate common enhancing malignant lesions of the brain. *AJNR. Am. J. Neuroradiol.* **32**, 1004–1010 (2011).
9. Leu, K. *et al.* Perfusion and diffusion MRI signatures in histologic and genetic subtypes of WHO grade II–III diffuse gliomas. *J. Neurooncol.* **134**, 177–188 (2017).
10. Kickingereder, P. *et al.* IDH mutation status is associated with a distinct hypoxia/angiogenesis transcriptome signature which is non-invasively predictable with rCBV imaging in human glioma. *Sci. Rep.* **5**, 1–9 (2015).
11. Sanvito, F., Castellano, A. & Falini, A. Advancements in neuroimaging to unravel biological and molecular features of brain tumors. *Cancers (Basel)*. **13**, 1–25 (2021).
12. Cho, N. S., Hagiwara, A., Sanvito, F. & Ellingson, B. M. A multi-reader comparison of normal-appearing white matter normalization techniques for perfusion and diffusion MRI in brain tumors. *Neuroradiology* **65**, 559–568 (2023).

13. Cindil, E. *et al.* Prediction of IDH Mutation Status in High-grade Gliomas Using DWI and High T1-weight DSC-MRI. *Acad. Radiol.* **29 Suppl 3**, S52–S62 (2022).
14. van Dijken, B. R. J. *et al.* Perfusion MRI in treatment evaluation of glioblastomas: Clinical relevance of current and future techniques. *J. Magn. Reson. Imaging* **49**, 11–22 (2019).
15. Prager, A. J. *et al.* Diffusion and perfusion MRI to differentiate treatment-related changes including pseudoprogression from recurrent tumors in high-grade gliomas with histopathologic evidence. *AJNR. Am. J. Neuroradiol.* **36**, 877–885 (2015).
16. Muto, M. *et al.* Dynamic susceptibility contrast (DSC) perfusion MRI in differential diagnosis between radionecrosis and neoangiogenesis in cerebral metastases using rCBV, rCBF and K2. *Radiol. Med.* **123**, 545–552 (2018).
17. Strauss, S. B., Meng, A., Ebani, E. J. & Chiang, G. C. Imaging Glioblastoma Posttreatment: Progression, Pseudoprogression, Pseudoresponse, Radiation Necrosis. *Radiologic Clinics of North America* **57**, 1199–1216 (2019).
18. Shin, K. E. *et al.* DCE and DSC MR perfusion imaging in the differentiation of recurrent tumour from treatment-related changes in patients with glioma. *Clin. Radiol.* **69**, e264–72 (2014).
19. Barajas, R. F. J. *et al.* Differentiation of recurrent glioblastoma multiforme from radiation necrosis after external beam radiation therapy with dynamic susceptibility-weighted contrast-enhanced perfusion MR imaging. *Radiology* **253**, 486–496 (2009).
20. Lee, M. D., Baird, G. L., Bell, L. C., Quarles, C. C. & Boxerman, J. L. Utility of Percentage Signal Recovery and Baseline Signal in DSC-MRI Optimized for Relative CBV Measurement for Differentiating Glioblastoma, Lymphoma, Metastasis, and Meningioma. *AJNR. Am. J. Neuroradiol.* **40**, 1445–1450 (2019).
21. Cindil, E. *et al.* Validation of combined use of DWI and percentage signal recovery-optimized protocol of DSC-MRI in differentiation of high-grade glioma, metastasis, and lymphoma. *Neuroradiology* **63**, 331–342 (2021).
22. Wang, F. *et al.* Improved performance of non-preloaded and high flip-angle dynamic susceptibility contrast perfusion-weighted imaging sequences in the presurgical differentiation of brain lymphoma and glioblastoma. *Eur. Radiol.* **33**, 8800–8808 (2023).
23. Neska-Matuszewska, M., Bładowska, J., Szaśiadek, M. & Zimny, A. Differentiation of glioblastoma multiforme, metastases and primary central nervous system lymphomas using multiparametric perfusion and diffusion MR imaging of a tumor core and a peritumoral zone-Searching for a practical approach. *PLoS One* **13**, e0191341 (2018).
24. Bao, S. *et al.* Differentiating between Glioblastoma and Primary CNS Lymphoma Using Combined Whole-tumor Histogram Analysis of the Normalized Cerebral Blood Volume and the Apparent Diffusion Coefficient. *Magn. Reson. Med. Sci. MRMS an Off. J. Japan Soc. Magn. Reson. Med.* **18**, 53–61 (2019).
25. Kickingereder, P. *et al.* Primary central nervous system lymphoma and atypical glioblastoma: multiparametric differentiation by using diffusion-, perfusion-, and susceptibility-weighted MR imaging. *Radiology* **272**, 843–850 (2014).
26. Chaganti, J., Taylor, M., Woodford, H. & Steel, T. Differentiation of Primary Central Nervous System Lymphoma and High-Grade Glioma with Dynamic Susceptibility Contrast-Derived Metrics: Pilot Study. *World Neurosurg.* **151**, e979–e987 (2021).
27. Boxerman, J. L. *et al.* Consensus recommendations for a dynamic susceptibility contrast MRI protocol for use in high-grade gliomas. *Neuro. Oncol.* **22**, 1262–1275 (2020).
28. Sanvito, F., Kaufmann, T. J., Cloughesy, T. F., Wen, P. Y. & Ellingson, B. M. Standardized brain tumor imaging protocols for clinical trials: current recommendations and tips for integration. *Front. Radiol.* **3**, (2023).
29. Leu, K., Boxerman, J. L. & Ellingson, B. M. Effects of MRI Protocol Parameters, Preload Injection Dose, Fractionation Strategies, and Leakage Correction Algorithms on the Fidelity of Dynamic-Susceptibility Contrast MRI Estimates of Relative Cerebral Blood Volume in Gliomas. *AJNR. Am. J. Neuroradiol.* **38**, 478–484 (2017).
30. Shiroishi, M. S. *et al.* A cross-sectional study to test equivalence of low- versus intermediate-flip angle dynamic susceptibility contrast MRI measures of relative cerebral blood volume in patients with high-grade gliomas at 1.5 Tesla field strength. *Front. Oncol.* **13**, 1156843 (2023).
31. Schmainda, K. M. *et al.* Moving Toward a Consensus DSC-MRI Protocol: Validation of a Low-Flip Angle Single-Dose Option as a Reference Standard for Brain Tumors. *AJNR. Am. J. Neuroradiol.* **40**, 626–633 (2019).
32. Boxerman, J. L., Paulson, E. S., Prah, M. A. & Schmainda, K. M. The effect of pulse sequence parameters and contrast agent dose on percentage signal recovery in DSC-MRI: implications for clinical applications. *AJNR. Am. J. Neuroradiol.* **34**, 1364–1369 (2013).
33. Ellingson, B. M. *et al.* Consensus recommendations for a standardized Brain Tumor Imaging Protocol in clinical trials. *Neuro. Oncol.* **17**, 1188–1198 (2015).
34. Schmiedeskamp, H. *et al.* Combined spin- and gradient-echo perfusion-weighted imaging. *Magn. Reson. Med.* **68**, 30–40 (2012).
35. Schmiedeskamp, H., Straka, M. & Bammer, R. Compensation of slice profile mismatch in combined spin- and gradient-echo echo-planar imaging pulse sequences. *Magn. Reson. Med.* **67**, 378–388 (2012).
36. Welker, K. *et al.* ASFNR recommendations for clinical performance of MR dynamic susceptibility contrast perfusion imaging of the brain. *Am. J. Neuroradiol.* **36**, E41–E51 (2015).
37. Stokes, A. M. *et al.* Evaluation of single bolus, dual-echo dynamic susceptibility contrast MRI protocols in brain tumor patients. *J. Cereb. blood flow Metab. Off. J. Int. Soc. Cereb. Blood Flow Metab.* **41**, 3378–3390 (2021).
38. Leu, K. *et al.* Improved Leakage Correction for Single-Echo Dynamic Susceptibility Contrast Perfusion MRI Estimates of Relative Cerebral Blood Volume in High-Grade Gliomas by Accounting for Bidirectional Contrast Agent Exchange. *AJNR. Am. J. Neuroradiol.* **37**, 1440–1446 (2016).
39. Boxerman, J. L., Schmainda, K. M. & Weisskoff, R. M. Relative cerebral blood volume maps corrected for contrast agent extravasation significantly correlate with glioma tumor grade, whereas uncorrected maps do not. *AJNR. Am. J. Neuroradiol.* **27**, 859–867 (2006).
40. Ellingson, B. M. *et al.* Recurrent glioblastoma treated with bevacizumab: contrast-enhanced T1-weighted subtraction maps improve tumor delineation and aid prediction of survival in a multicenter clinical trial. *Radiology* **271**, 200–210 (2014).
41. Schober, P., Boer, C. & Schwarte, L. A. Correlation Coefficients: Appropriate Use and Interpretation. *Anesth. Analg.* **126**, 1763–1768 (2018).

42. Koo, T. K. & Li, M. Y. A Guideline of Selecting and Reporting Intraclass Correlation Coefficients for Reliability Research. *J. Chiropr. Med.* **15**, 155–163 (2016).
43. Quarles, C. C., Gore, J. C., Xu, L. & Yankeelov, T. E. Comparison of dual-echo DSC-MRI- and DCE-MRI-derived contrast agent kinetic parameters. *Magn. Reson. Imaging* **30**, 944–953 (2012).
44. Wen, P. Y. *et al.* RANO 2.0: Update to the Response Assessment in Neuro-Oncology criteria for high- and low-grade gliomas in adults. *J. Clin. Oncol.* **41**, 5187–5199 (2023).
45. Aronen, H. J. & Perkiö, J. Dynamic susceptibility contrast MRI of gliomas. *Neuroimaging Clin. N. Am.* **12**, 501–523 (2002).
46. Henriksen, O. M. *et al.* High-Grade Glioma Treatment Response Monitoring Biomarkers: A Position Statement on the Evidence Supporting the Use of Advanced MRI Techniques in the Clinic, and the Latest Bench-to-Bedside Developments. Part 1: Perfusion and Diffusion Techniques. *Front. Oncol.* **12**, 810263 (2022).
47. Semmineh, N. B., Stokes, A. M., Bell, L. C., Boxerman, J. L. & Quarles, C. C. A Population-Based Digital Reference Object (DRO) for Optimizing Dynamic Susceptibility Contrast (DSC)-MRI Methods for Clinical Trials. *Tomogr. (Ann Arbor, Mich.)* **3**, 41–49 (2017).
48. Semmineh, N. B. *et al.* Optimization of Acquisition and Analysis Methods for Clinical Dynamic Susceptibility Contrast MRI Using a Population-Based Digital Reference Object. *AJNR. Am. J. Neuroradiol.* **39**, 1981–1988 (2018).
49. Stokes, A. M., Semmineh, N. B., Nespodzany, A., Bell, L. C. & Quarles, C. C. Systematic assessment of multi-echo dynamic susceptibility contrast MRI using a digital reference object. *Magn. Reson. Med.* **83**, 109–123 (2020).
50. Tofts, P. S. *et al.* Estimating kinetic parameters from dynamic contrast-enhanced T(1)-weighted MRI of a diffusable tracer: standardized quantities and symbols. *J. Magn. Reson. Imaging* **10**, 223–232 (1999).
51. Emblem, K. E. *et al.* Vessel architectural imaging identifies cancer patient responders to anti-angiogenic therapy. *Nat. Med.* **19**, 1178–1183 (2013).

Equation for $R_2^*(t)$ computed from the acquired two echoes:

(Suppl.Eq.1)

$$R_2^*(t) = \frac{1}{TE_2 - TE_1} \left[\ln \left(\frac{S_{TE1}(t)}{S_{TE2}(t)} \right) \right]$$

where:

- $R_2^*(t)$ [s^{-1}] is the transverse relaxation rate over time from the acquired dual-echo sequence (echo1 and echo2), which bears no T_1 -weighting;
- $S_{TE1}(t)$ and $S_{TE2}(t)$ are the signals of echo1 and echo2 over time;
- TE_1 and TE_2 are the TEs of echo1 and echo2 (respectively) in seconds as acquired in the dual-echo sequence (in our case, 0.014 s and 0.0341 s, respectively).

Equation for $R_1(t)$ computed from the acquired two echoes:

(Suppl.Eq.2)

$$R_1(t) = \frac{-1}{TR_{acquired}} \ln \left(\frac{1 - A}{1 - \cos(\alpha_{acquired}) * A} \right)$$

with:

$$A = \frac{1 - E_{10}}{1 - \cos(\alpha_{acquired}) * E_{10}} * \frac{T_1 w_{acquired}(t)}{T_1 w_{acquired}(0)}$$

with:

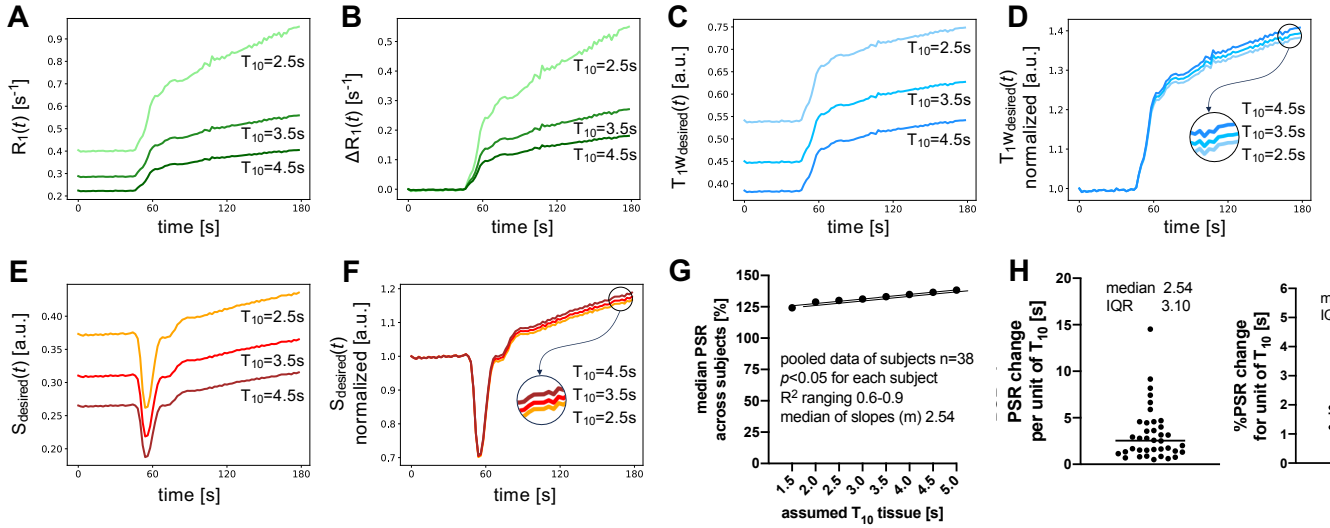
$$E_{10} = e^{\frac{-TR_{acquired}}{T_{10}}}$$

with:

$$T_1 w_{acquired}(t) = S_{TE1}(t) * \left(\frac{S_{TE1}(t)}{S_{TE2}(t)} \right)^{\frac{TE_1}{(TE_2 - TE_1)}}$$

where:

- $R_1(t)$ [s^{-1}] is the longitudinal relaxation over time;
- T_{10} is the fixed estimated pre-bolus quantitative T_1 for the tissue at 3T – we picked 5.0 s account for voxels containing fluid, even though contrast-enhancing tumor tissue reportedly has a shorter reported $T_{10} \sim 2.5s^{-1}$. This was necessary because in DSC T_{10} and $TR_{acquired}$ have the same order of magnitude, and a short T_{10} can result in the argument of the natural logarithm being <0 , which prevents the computation of $R_1(t)$. This is the reason why we were able to test shorter T_{10} when analyzing median *tumor* signals (**Suppl.Fig.1**), but not when generating voxel-wise whole brain datasets;
- $TR_{acquired}$ [s] is the acquired TR of the dynamic SAGE-EPI, in our case 2.0 s;
- $T_1 w_{acquired}(t)$ is the purely T_1 -weighted contribution to the signals of E1 and E2 of dynamic SAGE-EPI, obtained by extrapolating the estimated signal at $TE=0$ s;
- $T_1 w_{acquired}(0)$ is the prebolus $T_1 w$ contribution, computed by averaging the initial 10 timepoints of $T_1 w_{acquired}(t)$;
- $\alpha_{acquired}$ is the acquired flip angle (in our case, 90°);
- $S_{TE1}(t)$ and $S_{TE2}(t)$ are the signals of E1 and E2 (respectively) over time;
- TE_1 and TE_2 are the TEs of E1 and E2 (respectively) in seconds (in our case, 0.014 s and 0.0341 s, respectively).



Suppl. Fig. 1. Impact of the assumed tissue T_{10} on synthetic DSC. Differences in assumed T_{10} values cause pronounced differences in the estimated $R_1(t)$ and $\Delta R_1(t)$ curves, as seen in a representative case (A-B). However, when using the estimated $R_1(t)$ curve to synthesize the T_1w component of the desired signal, marked differences are appreciable only in the $T_1w_{\text{desired}}(t)$ curve expressed in absolute values, but not in the normalized $T_1w_{\text{desired}}(t)$ (C-D). As a consequence, in the desired synthetic DSC signal, too, the differences are appreciable only in the $S_{\text{desired}}(t)$ curve expressed in absolute values, but not in the normalized $S_{\text{desired}}(t)$ (E-F). Of note, a longer assumed T_{10} results in lower absolute values of $T_1w_{\text{desired}}(t)$ and $S_{\text{desired}}(t)$ throughout the curves, but in higher normalized values in the normalized curves. The fact that the normalized $S_{\text{desired}}(t)$ curve only minimally changes depending on T_{10} implies that the resulting rCBV and PSR calculations are robust with respect to the assumed T_{10} value, since both rCBV and PSR measurements depend on the shape of the normalized curve rather than on its absolute values. Indeed, analyses on median tumor synthetic DSC signal, performed on the whole cohort, showed that PSR values only slightly increase with a longer fixed T_{10} . Fitting a linear regression to each tumor (A, showing only the median observation of the cohort for each T_{10}), we obtained a distribution of slopes (m) with median 2.54 and interquartile range 3.10 (B). This means that a median of 2.54 %PSR overestimation should be expected for each second of increased T_{10} compared to the theoretical ground truth T_{10} .

Equation to adjust $R_2^*(t)$ and $R_1(t)$ to simulate preload administration (Suppl.Eq.3)

$$R_{1,\text{after_preload}}(t) = R_1(t) + [R_1(\text{final}) - R_1(0)]$$

$$R_{2,\text{after_preload}}^*(t) = R_2^*(t) + [R_2^*(\text{final}) - R_2^*(0)]$$

where:

- $R_1(t)$ [s^{-1}] and $R_2^*(t)$ [s^{-1}] are the previously computed longitudinal and transverse relaxation rate over time, respectively;
- $R_1(0)$ [s^{-1}] and $R_2^*(0)$ [s^{-1}] are the prebolus R_1 and R_2^* , computed by averaging the initial 10 timepoints of $R_1(t)$ and $R_2^*(t)$ – in case of $R_1(0)$, the value will be approximately the same as $1/T_{10}$ (i.e., R_{10}), where T_{10} is the fixed tissue T_1 from the literature;
- $R_1(\text{final})$ [s^{-1}] and $R_2^*(\text{final})$ [s^{-1}] are the postbolus R_1 and R_2^* , computed by averaging the final 10 timepoints of $R_1(t)$ and $R_2^*(t)$;
- $[R_1(\text{final}) - R_1(0)]$ [s^{-1}] and $[R_2^*(\text{final}) - R_2^*(0)]$ [s^{-1}] therefore represent the difference between a baseline relaxation rates without and with preload simulation;
- $R_{1,\text{after_preload}}(t)$ [s^{-1}] and $R_{2,\text{after_preload}}^*(t)$ [s^{-1}] are the adjusted $R_1(t)$ and $R_2^*(t)$ to simulate a preliminary preload administration. If the simulation of preload administration is desired, the “after preload” adjusted values should be used in the subsequent equations.

Equation for simulated $T_2^*w(t)$ contribution with desired pulse sequence parameters: (Suppl.Eq.4)

$$T_2^*w_{\text{desired}}(t) = e^{-R_2^*(t) \cdot TE_{\text{desired}}}$$

where:

- $R_2^*(t)$ [s^{-1}] is the previously computed transverse relaxation rate over time;
- TE_{desired} [s] is the desired arbitrary TE (e.g., 0.030 s).

Equation for simulated $T_1w(t)$ contribution with desired pulse sequence parameters:

(Suppl.Eq.5)

$$T_1w_{\text{desired}}(t) = \sin(\alpha_{\text{desired}}) * \frac{1 - e^{-TR_{\text{desired}}*R_1(t)}}{1 - \cos(\alpha_{\text{desired}}) * e^{-TR_{\text{desired}}*R_1(t)}}$$

where:

- α_{desired} is the desired arbitrary FA (for instance, 60° or 30°);
- TR_{desired} [s] is the desired arbitrary TR (for instance, 1.5 or 1.0 s);
- $R_1(t)$ [s^{-1}] is the previously computed longitudinal relaxation rate over time;

Equation for the synthetic time-intensity curve $S_{\text{desired}}(t)$ with desired pulse sequence parameters:

(Suppl.Eq.6)

$$S_{\text{desired}}(t) = \mu_0 * T_2^*w_{\text{desired}}(t) * T_1w_{\text{desired}}(t)$$

where:

- $T_2^*w_{\text{desired}}(t)$ is the previously computed T_2^* -weighted contribution of the signal with the desired arbitrary pulse sequence parameters;
- $T_1w_{\text{desired}}(t)$ is the previously computed T_1 -weighted contribution of the signal with the desired arbitrary pulse sequence parameters;
- μ_0 is a constant representing bulk magnetization and coil coupling and impedance, μ_0 can be set to 1 for simplicity, because the purpose of this equation in the present study is to compute the percentage of signal recovery (PSR) and relative cerebral blood volume (rCBV), and μ_0 cancels out during such computation (see below).

Equation for rCBV computation

(Suppl.Eq.7)

$$rCBV = \int \Delta R_{2,\text{single_echo}}^*(t) dt$$

when $\Delta R_{2,\text{single_echo}}^*(t) \geq 0$

as in Stokes *et al.* ²

where:

$$\Delta t = TR_{\text{acquired}}$$

and:

$$\Delta R_{2,\text{single_echo}}^*(t) = -\frac{\ln\left(\frac{S_{\text{desired}}(t)}{S_{\text{desired}}(0)}\right)}{TE_{\text{desired}}}$$

where:

- $S_{\text{desired}}(0)$ is the pre-bolus signal with the desired pulse sequence parameters, computed by averaging the initial 10 timepoints of $S_{\text{desired}}(t)$.

Note that $\Delta R_{2,\text{single_echo}}^*(t)$ can undergo model-based leakage correction prior to integration.

See **Suppl.Fig.2A-B** for a graphic representation of the integration without and with leakage correction.

Finally, rCBV was normalized to the contralateral white matter to obtain nrCBV.

Equation for PSR computation

(Suppl.Eq.8)

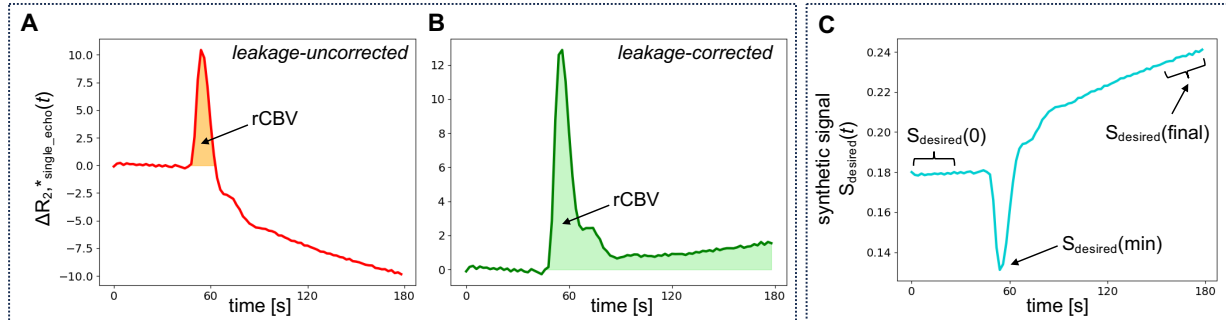
$$PSR\% = \frac{S_{\text{desired}}(\text{final}) - S_{\text{desired}}(\text{min})}{S_{\text{desired}}(0) - S_{\text{desired}}(\text{min})} * 100\%$$

as in Lee *et al.* ³

where:

- $S_{\text{desired}}(\text{final})$ is the post-bolus signal with the desired pulse sequence parameters, computed by averaging the final 10 timepoints of $S_{\text{desired}}(t)$;
- $S_{\text{desired}}(\text{min})$ is the minimum signal observed in $S_{\text{desired}}(t)$;
- $S_{\text{desired}}(0)$ is the pre-bolus signal with the desired pulse sequence parameters, computed by averaging the initial 10 timepoints of $S_{\text{desired}}(t)$.

See **Suppl.Fig.2C** for a graphic representation of $S_{\text{desired}}(\text{final})$, $S_{\text{desired}}(\text{min})$, $S_{\text{desired}}(0)$:



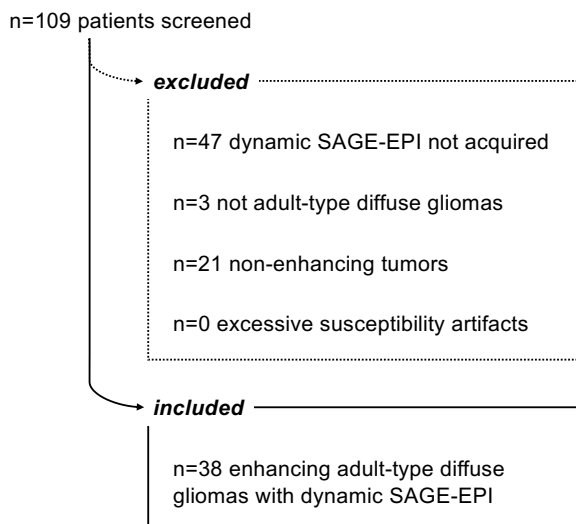
Suppl.Fig.2. Graphic representation of rCBV (A, B) and PSR (C).

Equation to compute the % variation in ranks across protocols (Suppl.Eq.9)

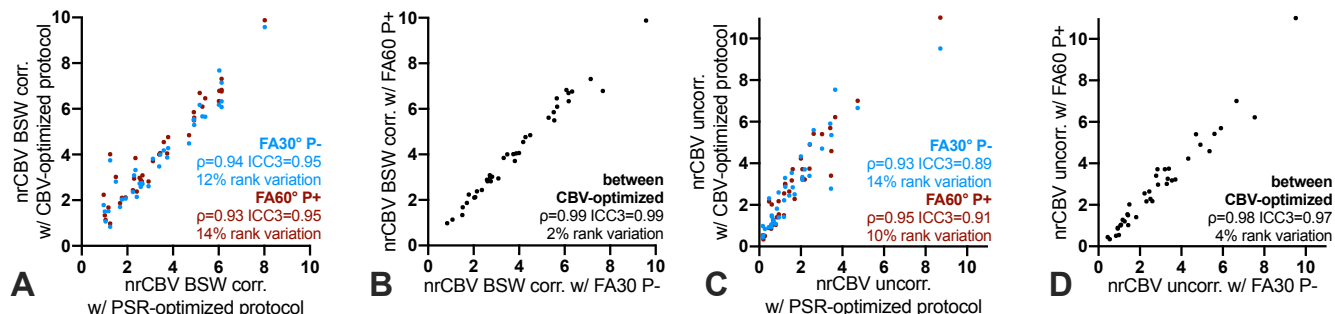
$$\text{variation in ranks (\%)} = (1 - \rho^2) * 100\%$$

where:

- ρ is the Spearman's correlation coefficient between a certain DSC metric (i.e., PSR or nrCBV) calculated with a certain synthetic protocol (e.g., a CBV-optimized protocol: FA 30°, TE 30ms, TR 1.5s, P-) and the same DSC metric calculated with another synthetic protocol (e.g., PSR-optimized protocol FA 90°, TE 30ms, TR 1.5s, P-).
- the variation in ranks (%) reflects the change in the observed order statistics due to the protocol change. Indeed, the Spearman's ρ calculated between DSC metrics corresponds to the Pearson's correlation coefficient (r) calculated between the ranks of such DSC metrics. The coefficient of determination ($R^2 = r * r$, ranging 0 to 1) can be interpreted as the fraction of the variability in the dataset that is explained by the linear regression model. Therefore, $1 - R^2$ represents the residual variability in the dataset that is *not* explained by the model. Since the only source of variability in our analysis is the change in the protocol, $1 - \rho^2$ can be interpreted as the variation in ranks ascribable to protocol changes.



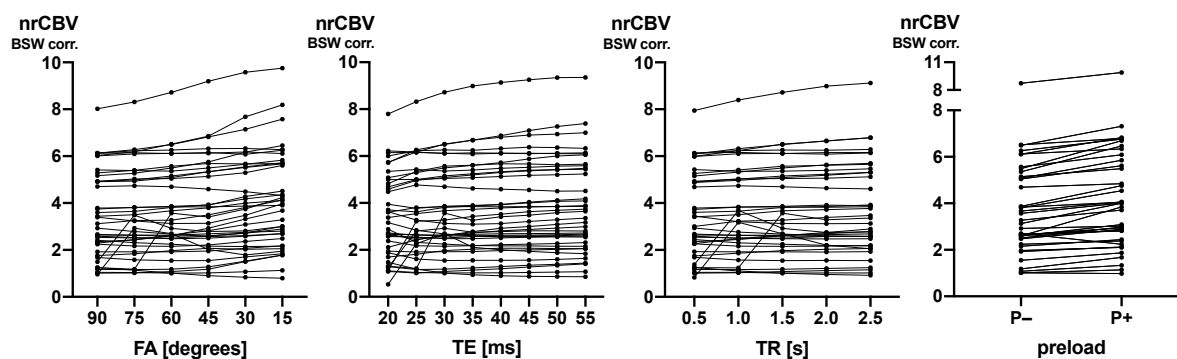
Suppl.Fig.3. Flowchart of patients included and excluded from the study.



Suppl. Fig. 4. nrCBV values with BSW leakage correction (A, B) showed comparable results to bidirectional leakage correction in terms of ranks consistency (ρ) and value agreement (ICC). Uncorrected nrCBV (C, D) had worse value agreement (ICC) between protocols compared to its leakage-corrected counterparts, especially when comparing PSR-optimized and CBV-optimized protocols.

Suppl. Tab. 1. Clinical and imaging characteristics of the external cohorts.

External Cohorts				
	GBM cohort from Cindil et al. ⁴	PCNSL cohort from Cindil et al. ⁴	PCNSL cohort from Wang et. al ⁵ (non-preloaded)	PCNSL cohort from Wang et. al ⁵ (preloaded)
Sample size	60	15	50	77
Age	50±16 years	61±15 years	59±12 years	
Diagnosis	Histopathological	Histopathological	Histopathological	Histopathological
Treatment status	Treatment-naïve	Treatment-naïve	Treatment-naïve	Treatment-naïve
Tumor component analyzed	Contrast-enhancing component	Contrast-enhancing component	Contrast-enhancing component	Contrast-enhancing component
PSR values	95.3±20.1%	164.1±37.0%	163.0±90.0%	70.0±71.0%
PSR extraction method	Multiple 2D ROIs	Multiple 2D ROIs	3D segmentation	3D segmentation
DSC parameters	FA 90° TE 30 TR 1.5 P-	FA 90° TE 30 TR 1.5 P-	FA 90° TE 30 TR 1.6 P-	FA 90° TE 30 TR 1.6 P+
DSC duration	1min 23s	1min 23s	1min 36s	1min 36s



Suppl. Fig. 5. The impact of acquisition factors on nrCBV values with BSW leakage correction was overall similar to nrCBV with bidirectional leakage correction.

STROBE Statement—checklist of items that should be included in reports of observational studies

	Item No	Recommendation	Checkmark
Title and abstract	1	(a) Indicate the study’s design with a commonly used term in the title or the abstract	✓
		(b) Provide in the abstract an informative and balanced summary of what was done and what was found	✓
Introduction			
Background/rationale	2	Explain the scientific background and rationale for the investigation being reported	✓
Objectives	3	State specific objectives, including any prespecified hypotheses	✓
Methods			
Study design	4	Present key elements of study design early in the paper	✓
Setting	5	Describe the setting, locations, and relevant dates, including periods of recruitment, exposure, follow-up, and data collection	✓
Participants	6	(a) <i>Cohort study</i> —Give the eligibility criteria, and the sources and methods of selection of participants. Describe methods of follow-up	n/a
		<i>Case-control study</i> —Give the eligibility criteria, and the sources and methods of case ascertainment and control selection. Give the rationale for the choice of cases and controls	n/a
		<i>Cross-sectional study</i> —Give the eligibility criteria, and the sources and methods of selection of participants	✓
		(b) <i>Cohort study</i> —For matched studies, give matching criteria and number of exposed and unexposed <i>Case-control study</i> —For matched studies, give matching criteria and the number of controls per case	
Variables	7	Clearly define all outcomes, exposures, predictors, potential confounders, and effect modifiers. Give diagnostic criteria, if applicable	✓
Data sources/ measurement	8*	For each variable of interest, give sources of data and details of methods of assessment (measurement). Describe comparability of assessment methods if there is more than one group	✓
Bias	9	Describe any efforts to address potential sources of bias	✓
Study size	10	Explain how the study size was arrived at	✓
Quantitative variables	11	Explain how quantitative variables were handled in the analyses. If applicable, describe which groupings were chosen and why	✓
Statistical methods	12	(a) Describe all statistical methods, including those used to control for confounding	✓
		(b) Describe any methods used to examine subgroups and interactions	n/a
		(c) Explain how missing data were addressed	n/a
		(d) <i>Cohort study</i> —If applicable, explain how loss to follow-up was addressed <i>Case-control study</i> —If applicable, explain how matching of cases and controls was addressed	n/a
		<i>Cross-sectional study</i> —If applicable, describe analytical methods taking account of sampling strategy	n/a
		(e) Describe any sensitivity analyses	n/a

Continued on next page

Results		Checkmark	
Participants	13*	(a) Report numbers of individuals at each stage of study—eg numbers potentially eligible, examined for eligibility, confirmed eligible, included in the study, completing follow-up, and analysed	✓
		(b) Give reasons for non-participation at each stage	✓
		(c) Consider use of a flow diagram	✓
Descriptive data	14*	(a) Give characteristics of study participants (eg demographic, clinical, social) and information on exposures and potential confounders	✓
		(b) Indicate number of participants with missing data for each variable of interest	n/a
		(c) <i>Cohort study</i> —Summarise follow-up time (eg, average and total amount)	n/a
Outcome data	15*	<i>Cohort study</i> —Report numbers of outcome events or summary measures over time	n/a
		<i>Case-control study</i> —Report numbers in each exposure category, or summary measures of exposure	n/a
		<i>Cross-sectional study</i> —Report numbers of outcome events or summary measures	✓
Main results	16	(a) Give unadjusted estimates and, if applicable, confounder-adjusted estimates and their precision (eg, 95% confidence interval). Make clear which confounders were adjusted for and why they were included	✓
		(b) Report category boundaries when continuous variables were categorized	✓
		(c) If relevant, consider translating estimates of relative risk into absolute risk for a meaningful time period	n/a
Other analyses	17	Report other analyses done—eg analyses of subgroups and interactions, and sensitivity analyses	✓
Discussion			
Key results	18	Summarise key results with reference to study objectives	✓
Limitations	19	Discuss limitations of the study, taking into account sources of potential bias or imprecision. Discuss both direction and magnitude of any potential bias	✓
Interpretation	20	Give a cautious overall interpretation of results considering objectives, limitations, multiplicity of analyses, results from similar studies, and other relevant evidence	✓
Generalisability	21	Discuss the generalisability (external validity) of the study results	✓
Other information			
Funding	22	Give the source of funding and the role of the funders for the present study and, if applicable, for the original study on which the present article is based	✓

References for Supplemental Material

1. Hattingen E, Müller A, Jurcoane A, et al. Value of quantitative magnetic resonance imaging T1-relaxometry in predicting contrast-enhancement in glioblastoma patients. *Oncotarget* 2017;8:53542–51.
2. Stokes AM, Bergamino M, Alhilali L, et al. Evaluation of single bolus, dual-echo dynamic susceptibility contrast MRI protocols in brain tumor patients. *J Cereb blood flow Metab Off J Int Soc Cereb Blood Flow Metab* 2021;41:3378–90.
3. Lee MD, Baird GL, Bell LC, et al. Utility of Percentage Signal Recovery and Baseline Signal in DSC-MRI Optimized for Relative CBV Measurement for Differentiating Glioblastoma, Lymphoma, Metastasis, and Meningioma. *AJNR Am J Neuroradiol* 2019;40:1445–50.
4. Cindil E, Sendur HN, Cerit MN, et al. Validation of combined use of DWI and percentage signal recovery-optimized protocol of DSC-MRI in differentiation of high-grade glioma, metastasis, and lymphoma. *Neuroradiology* 2021;63:331–42.
5. Wang F, Zhou X, Chen R, et al. Improved performance of non-preloaded and high flip-angle dynamic susceptibility contrast perfusion-weighted imaging sequences in the presurgical differentiation of brain lymphoma and glioblastoma. *Eur Radiol* 2023;33:8800–8.